Monthly Notices
of the
ROYAL ASTRONOMICAL SOCIETY

Mon. Not. R. Astron. Soc. **421,** 224–234 (2012) doi:10.1111/j.1365-2966.2011.20295.x

A high signal-to-noise ratio map of the Sunyaev–Zel'dovich increment at 1.1-mm wavelength in Abell 1835

P. D. Mauskopf,[1⋆] P. F. Horner,[1] J. Aguirre,[2] J. J. Bock,[3] E. Egami,[4] J. Glenn,[5] S. R. Golwala,[6] G. Laurent,[5] H. T. Nguyen[3] and J. Sayers[6]

[1]*Cardiff School of Physics and Astronomy, Cardiff University, Queens Buildings, The Parade, Cardiff CF24 3AA*
[2]*Department of Physics and Astronomy, University of Pennsylvania, 209 South 33rd Street, Philadelphia, PA 19104, USA*
[3]*Jet Propulsion Laboratory, California Institute of Technology, 4800 Oak Grove Drive, Pasadena, CA 91109, USA*
[4]*Department of Astronomy/Steward Observatory, 933 North Cherry Avenue, Rm. N204, Tucson, AZ 85721-0065, USA*
[5]*Center for Astrophysics and Space Astronomy, Department of Astrophysical and Planetary Sciences, University of Colorado, 389 UCB, Boulder, CO 80309, USA*
[6]*Division of Physics, Mathematics & Astronomy, California Institute of Technology, Mail Code 59-33, Pasadena, CA 91125, USA*

Accepted 2011 November 29. Received 2011 October 13; in original form 2011 July 7

ABSTRACT

We present an analysis of an 8-arcmin diameter map of the area around the galaxy cluster Abell 1835 from jiggle-map observations at a wavelength of 1.1 mm using the Bolometric Camera (Bolocam) mounted on the Caltech Submillimeter Observatory (CSO). The data are well described by a model including a extended Sunyaev–Zel'dovich (SZ) emission from the cluster gas plus emission from the cluster central galaxy and two bright background submm galaxies magnified by the gravitational lensing of the cluster. We measure flux densities of the two bright point sources in the field: SMM J14011+0252 and SMM J14009+0252 to be $6.5 \pm 2.0 \pm 0.8$ and $11.3 \pm 1.9 \pm 1.3$ mJy, respectively. Fitting the map to a sky model consisting of the point sources and the SZ emission from the cluster gas with a beta model density profile with parameters, $\theta_c = 33.6$ arcsec and $\beta = 0.69$, we find the peak surface brightness of the SZ emission to be $I_c = 3.73 \pm 0.45 \pm 0.60 \times 10^{-21}$ W m^{-2}sr^{-1} Hz^{-1}, where the first error is the statistical uncertainty in the fit and the second error represents the calibration uncertainty and additional systematics. Assuming zero cluster peculiar velocity and an X-ray temperature of $T_e = 9$ keV, this surface brightness corresponds to a central Comptonization of $y_0 = (4.41 \pm 0.53 \pm 0.70) \times 10^{-4}$. The cluster image represents one of the highest significance SZ detections of a cluster in the positive region of the thermal SZ spectrum to date. We compare the measured central intensity at 1.1 mm to other SZ measurements of Abell 1835 at different wavelengths to obtain values for $y_0 = (3.58 \pm 0.28) \times 10^{-4}$ and the cluster peculiar velocity $v_z = -538 \pm 414$ km s^{-1}.

Key words: methods: data analysis – techniques: radial velocities – galaxies: clusters: individual: Abell 1835 – cosmic background radiation – submillimetre: galaxies.

1 INTRODUCTION

The Sunyaev–Zel'dovich (SZ) effect (Sunyeav & Zel'dovich 1970) is the distortion of the cosmic microwave background (CMB) spectrum due to interactions between CMB photons and hot electrons along the line of sight between the surface of last scattering and an observer. The primary source for the SZ effect is hot gas which makes up the intracluster medium (ICM) of massive galaxy clusters (Birkinshaw 1999; Carlstrom, Holder & Reese 2002; Rephaeli, Sadeh & Shimon 2005). The shape of the SZ spectral distortion from a galaxy cluster has contributions from two effects: a thermal effect and a kinematic effect. The thermal effect is observed as a decrement in the apparent brightness of the CMB towards a galaxy cluster at low frequencies and an increment at high frequencies with a crossover point at a frequency that depends on the gas temperature (217 GHz for a non-relativistic gas). The kinematic effect has the spectral dependence of a temperature shift in the CMB producing a change in apparent brightness with the same sign at all frequencies. The two effects can therefore be distinguished from each other with measurements at multiple frequencies.

Measurements of the amplitude of the SZ thermal distortion towards a cluster can be combined with measurements of the X-ray emission from the ICM to determine the angular diameter distance, d_A, which depends on cluster redshift and cosmological parameters (Birkinshaw, Hughes & Arnaud 1991). Estimates of the Hubble

⋆E-mail: Philip.Mauskopf@astro.cf.ac.uk

constant have been made using this technique for a number of clusters (e.g. Jones 1995; Grainge 1996; Holzapfel et al. 1997; Tsuboi et al. 1998; Mauskopf et al. 2000; Battistelli et al. 2003; Reese 2003; Udomprasert et al. 2004; Bonamente et al. 2006) and can be used to constrain cosmological models. In addition, because the integrated SZ flux density from a cluster with a given mass is almost independent of redshift, SZ surveys can provide mass-limited cluster counts relatively unbiased in redshift space compared to other cluster survey methods. The evolution of the number counts of clusters with redshift depends strongly on the evolution of the so-called dark energy or cosmological constant and therefore SZ surveys have been identified as one of the key probes of the nature of dark energy (e.g. Diego et al. 2002; Weller, Bettye & Kneissl 2002; DeDeo, Spergel & Trac 2005; Albrecht et al. 2006; Bhattacharya & Kosowsky 2007). A number of dedicated SZ surveys are already producing results including the Atacama Cosmology Telescope and the South Pole Telescope (Hincks et al. 2009; Plagge et al. 2009; High et al. 2010; Marriage et al. 2010; Vanderlinde et al. 2010; Williamson et al. 2011).

Most of the SZ detections reported to date have been made at low frequencies (<220 GHz) corresponding to the SZ decrement. Follow-up imaging or spectroscopic measurements of known clusters at higher frequencies corresponding to the SZ increment can improve the precision in the measurement of the kinematic SZ effect and constrain sources of contamination in the low-frequency data. However, at higher frequencies there is typically more emission from dusty galaxies including background high-redshift galaxies amplified by the gravitational lensing of the cluster and increased atmospheric contamination from ground-based telescopes relative to the SZ signal. Accurate measurement of the SZ increment requires a combination of angular resolution sufficient to resolve and remove point sources combined with high sensitivity and control of systematics necessary to detect the more diffuse SZ signal.

This paper presents analysis of observations of the galaxy cluster Abell 1835 using the Bolometric Camera (Bolocam) mounted on the Leighton telescope at the Caltech Submillimeter Observatory (CSO), situated on the summit of Mauna Kea, Hawaii. We also compare the results of this analysis with other sets of data taken at different wavelengths. Abell 1835 is one of the most luminous clusters observed in the *ROSAT* catalogue. It is also known to contain two lensed submm point sources, SMM J14009+0252 and SMM J14011+0252 (see e.g. Ivison et al. 2000; Zemcov et al. 2007).

The paper is organized as follows. Section 2 describes the observations with the Bolocam instrument. Section 3 describes the analysis pipeline developed for processing the data. Section 4 describes the modelling of the data and the determination of the characteristic parameters of the model (as well as the errors in their values), and Section 5 discusses the results of the analysis of the Bolocam data and their combination with other literature results.

2 OBSERVATIONS

The data reported here consist of approximately 12.5 h of observations at 1.1 mm (268 GHz) with the Bolocam instrument mounted at the Cassegrain focus of the 10.4-m Leighton telescope at the CSO from 2006 January 28 to February 5. Bolocam consists of an array of 105 operational neutron transmutation doped (NTD) germanium spiderweb bolometers which can be configured to observe at 1.1, 1.4 or 2.1 mm (Glenn et al. 1998; Haig et al. 2004). The detectors are cooled to 260 mK to allow the array to operate close to the photon background limit at 1.1 mm. The Bolocam array has a field of view of 7.5 arcmin, and the beam full width at half-maximum (FWHM) is 31 arcsec at 1.1 mm (and ∼60 arcsec at 2.1 mm). The principal science targets for the instrument include star-forming regions in the galaxy, blank-field surveys for dusty extragalactic point sources, blank-field SZ cluster surveys and pointed observations of galaxy clusters.

The majority of observations with Bolocam use raster scanning or lissajous scanning where the entire telescope is constantly in motion modulating the array position on the sky. The data presented in this paper were taken using jiggle mapping. Jiggle mapping uses a combination of chopping the secondary mirror from side-to-side in azimuth and nodding the telescope or changing the position of the primary mirror boresight in both azimuth and elevation during an observation. For a single jiggle position, the main telescope beam moves in azimuth from being 'on-source' (imaging the region of the target and chopping away from it) to 'off-source' (imaging a nearby region of blank sky and chopping on to the target), then returns to being 'on-source' once again (see Fig. 1). A jiggle map consists of a set of 16 on-off-on jiggle positions corresponding to 16 different azimuth and elevation offset positions centred around the astronomical target designed to produce a fully Nyquist sampled image.

The intensity of emission at 1.1 mm at the CSO from foreground sources including the warm telescope and water vapour in the atmosphere is equivalent to a brightness temperature of ≈60 K in

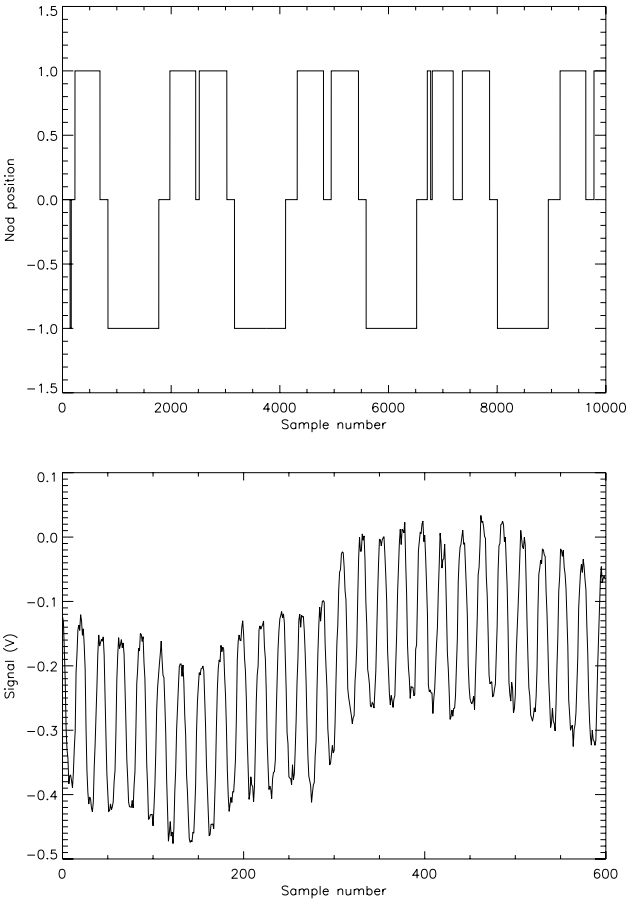

Figure 1. Nodding and acquisition pattern from telescope status data (top). A value of +1 implies the telescope is 'on-source', whereas a value of −1 is when the telescope is 'off-source'. A signal level of zero indicates that the telescope position is not coincident with the requested boresight position (usually while the dish is moving to a different location on the sky). A sample of the raw data demonstrating the chopping is also shown (bottom).

the sky conditions for these observations (average optical depth at 275 GHz ≈ 0.1) compared to a typical SZ cluster peak brightness temperature of tens to hundreds of μK and a detector sensitivity of a few mK in one second of integration. The variation in brightness of the sky emission (sky noise) dominates the system noise at low frequencies (<1 Hz). The sky noise is well described by a spatial power spectrum that rises steeply at large angular scales and is modulated by the wind (Sayers et al. 2010). Since the sky noise is highly correlated on small angular scales and short time-scales, it is possible to reduce the sky noise to a level below the detector noise by modulating the telescope beam on the sky between two nearby positions as long as the time for the beam to move between the two positions is sufficiently fast. This sky modulation is usually achieved during Bolocam observations with fast scanning of the telescope primary mirror with a maximum scan speed of approximately 240 arcsec s^{-1}. In the observations described in this paper, we instead modulated the beam by constantly chopping the secondary mirror back and forth while the main telescope boresight remained fixed. Care must be taken to ensure that the chop throw (i.e. the maximum angular displacement of the secondary during the chop) is large enough that the off beam does not contain signal from the source itself. For this reason, jiggle mapping is not optimal for imaging extended sources, but is well suited for observing point sources.

The chop frequency for this data set was 2.25 Hz, giving a chop period of ~0.44 s (compared to a sampling rate of 0.02 s). The chop throw and the displacement between on and off beams during the nods was 90 arcsec in azimuth. The telescope remained in the 'on' or 'off' positions for an integration time of approximately 10 s each. The full set of data consisted of 15 individual sets of observations of approximately 50 min each. The observations were separated by shorter observations of planets and other sources with known position and flux density, which could be used for the calibration and pointing corrections. From the noise in the final maps, we estimate a mapping speed for this data set to be 4 arcmin^2 Jy^{-2} h^{-1}, comparable to the mapping speed obtained for raster scan and lissajous scan observations (e.g. Enoch et al. 2006).

3 ANALYSIS PIPELINE

This paper reports the first results from Bolocam using jiggle mapping. The analysis pipeline used is a modification of the standard Bolocam pipeline used for reducing raster and lissajous scanned data (Laurent et al. 2005). In this paper we describe the modifications made for analysing the jiggle-map data.

In the standard pipeline, the raw time-stream data are separated into data vectors representing the signal from individual bolometers during specific observations (sliced) and bright pixel spikes from cosmic rays are flagged and removed (despiked). The next step is data cleaning or removal of sky noise. For the jiggle-map data, we construct a sky noise template from an average of the bolometer signals which we then subtract from each individual detector data vector (average subtraction). This removes atmospheric fluctuations that are correlated across the detector array without removing flux from astronomical sources that are small compared to the field of view of the array. Restricting the atmospheric removal to average subtraction allows for accurate simulation and modelling of the effects of the data cleaning on detected signals from astronomical sources. For data taken with raster scanning or lissajous scanning, a more complicated subtraction method using principle component analysis (PCA) can be used in order to further reduce the sky noise (Laurent et al. 2005).

Sky noise removal also removes some of the astronomical signal and introduces a 'transfer function' which generally reduces the observed flux density and spatial distribution of sources in the data. For a given scan strategy and sky noise cleaning algorithm, the transfer function can be calculated by generating a simulated time stream from an ideal source model and putting it through the same analysis pipeline as on the data. This has been done with lissajous and raster scanned data for both the PCA sky noise removal method (Laurent et al. 2005) and for average subtraction (Sayers et al. 2011). For the jiggle-map data, the transfer function is dominated by the effect of the chopping of the secondary mirror which effectively filters signals on the sky parallel to the chop direction with sizes larger than the chop throw. We perform the same analysis on a simulated source model to compute the transfer function of the jiggle-map data for the observations of Abell 1835. This requires a source model which includes both the SZ effect from the galaxy cluster and emission from dusty point sources. The detailed modelling is described in Section 4.

At the chop frequency of 2.25 Hz, the residual sky noise is generally smaller than the detector noise. Therefore, the use of average subtraction or any other sky noise removal in addition to the demodulation of the chop is not necessary. We include the average subtraction module in the pipeline primarily because it removes a low-frequency baseline from the data which allows simple visual comparison between the data and the reference signal from the chopper position which is used to lock in to the secondary mirror modulation.

The remainder of the analysis pipeline for the jiggle-map data involves the following main elements: (i) deconvolving the chopping and nodding sequence, (ii) determinating of pointing corrections for each observation, (iii) calibrating the maps from each observation and (iv) co-adding the maps to obtain a final image.

3.1 Deconvolving the chopping and nodding sequence

For each 15-min observation, we fit the time-stream data for the chopper position to the raw voltage signals from the detectors to correct for a phase difference or time delay between the chopper data and bolometer data. The bolometer signals exhibit optical modulation in phase with the chopper modulation (Fig. 1b) due to small differences in the emission from the telescope for different secondary and primary mirror illumination patterns. Phase differences between the chopper position time stream and the bolometer raw data can arise from the detectors, the analogue readout chain and the data acquisition. The finite bolometer time constants combined with the low pass filtering in the signal conditioning electronics introduce a fixed time shift in each bolometer raw data stream with respect to the chopper position of 40–50 ms or approximately two time samples as well as a small reduction in signal amplitude. We assume that the attenuation in signal amplitude is the same for the observations of faint point sources as for the bright calibration sources. Time delays in the sensor electronics and data acquisition system give an additional shift between the bolometer data and chopper data of approximately four samples. We monitor this delay by sampling the telescope TTL signals through the same analogue to digital converters as the detector signals and find that they are stable at the level of a single sample over the observing run.

We use a set of TTL signals monitoring the telescope status to identify subsections of the raw time-stream data corresponding to the 16 different jiggle positions of the telescope main boresight and discard data corresponding to times when the telescope is moving between positions. For each jiggle position, the telescope also

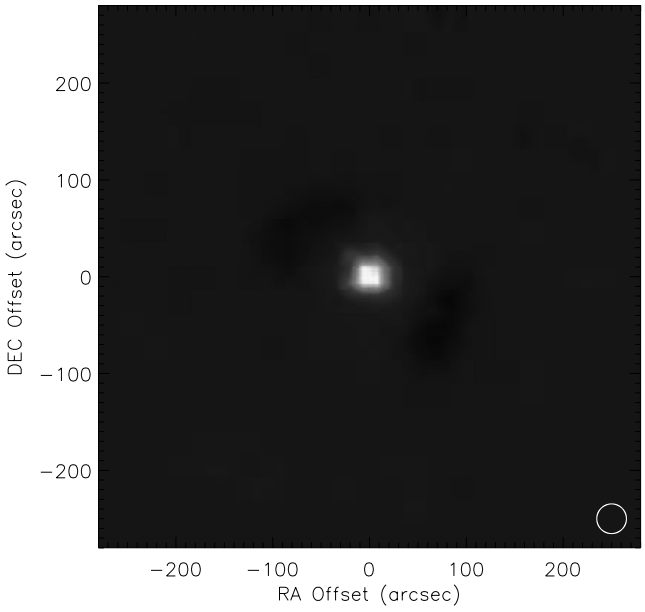

Figure 2. Bolocam jiggle map of the point source J1337−129. The pixel size is 15 arcsec in the map. The shape of the chopped beam pattern for a point source consists of a central positive lobe and two negative lobes. The negative lobes are spread out over a section of an annulus around the central lobe due to the fact that the chop is aligned in azimuth and this direction rotates with respect to the sky coordinates during the course of the observations included in this map.

undergoes a nodding sequence (Fig. 1a) or switching between two positions (left and right or on-source and off-source) of the main telescope boresight separated in azimuth by the same angular separation as the chop throw. We select an equal number of data points in each nodding position (left and right) to compute the amplitude of the chopped signal by fitting the data to a sine wave with the same frequency as the chop. We discard a small fraction of the data (<3 per cent) at the beginning and end of each nodding period. We then compute the difference between the amplitudes of the chopped signal in both nodding positions and obtain a signal and error for each jiggle position. This double difference due to the combination of chopping and nodding gives an effective beam pattern for each detector corresponding to a central positive lobe with a FWHM of 31 arcsec limited by the diffraction-limited optics of the telescope and two negative lobes on either side of the central lobe in azimuth separated by the chop throw of 90 arcsec with the same shape as the central lobe but half the amplitude (Fig. 2).

3.2 Pointing

The telescope pointing is controlled via a feedback loop using a set of encoders which record the telescope azimuth and elevation. During a jiggle-map observation, the telescope is commanded to point towards the selected astronomical target and cycle through a pre-programmed set of offsets in celestial coordinates (RA and Dec.). Due to thermal and gravitational deformations of the telescope as well as the mechanical flexing of the Bolocam receiver mount, there are offsets in azimuth and elevation between the commanded position and the actual main beam position which vary as a function of time and direction of the boresight. These offsets translate into azimuth and elevation dependent corrections to the reconstructed RA and Dec. in an observation. We determine these pointing corrections from observations of bright point sources located close to the main astronomical target obtained roughly every 20 min in between science observations.

Each pointing source is observed with an observing strategy consisting of a 10-min jiggle pattern with eight positions of the telescope boresight rather than the 16 positions used for the primary astronomical targets. We use the same method for deconvolving the chopper signals as described in the previous section to reduce the pointing data. We then make maps of the pointing sources from the deconvolved data using raw (uncorrected) pointing data and measure the reconstructed coordinates of the centre of emission for each pointing source using a simple χ^2 fit for the chopped beam to the data. We determine the pointing offset in azimuth and elevation for each map from the difference between the observed centre of emission and the known position of the pointing source. The resulting corrections to the fiducial pointing model coordinates are smaller than 10 arcsec with an rms of 3 arcsec. We use these offsets to correct the coordinates of the telescope boresight during observations of the science targets. Offsets in azimuth and elevation for each pixel in the focal plane from the telescope boresight are measured from individual bolometer maps of bright sources. These pixel offsets are consistent between Bolocam observing runs to within measurement accuracy (<3 arcsec).

3.3 Calibration

Calibration of Bolocam data requires scaling the raw time-stream data for each bolometer by a time-varying calibration factor. The Bolocam bolometers are biased with an AC current at a frequency of approximately 130 Hz. The raw bolometer output is an AC voltage which is demodulated to produce a raw DC-coupled time-stream data in the form of a voltage which is proportional to the resistance of the bolometer. This output DC level and the resistance of the bolometer depend on both the responsivity, S(V/W), of the bolometers and the attenuation of the astronomical signal by the atmosphere in such a way that there is a unique calibration scale factor for each value of the bolometer resistance or DC level.

There are two dominant sources of changes to the calibration during an observation: (i) variation of the responsivity of the bolometers due to changes in optical loading from atmospheric emission and (ii) attenuation of the astronomical signal by the atmosphere. For the conditions during the observations of Abell 1835, both the optical emission and attenuation were linearly proportional to the optical depth, τ. When the optical depth of the atmosphere increases, the corresponding emission from the atmosphere (sky loading) increases and the operating temperature of the bolometer also increases. The NTD Ge thermometers used in Bolocam bolometers have a negative temperature coefficient so that a higher operating temperature corresponds to a lower bolometer resistance and therefore a lower responsivity, S, to optical power. For small changes in τ,

$$S(\mathrm{V/W}) \propto R(\Omega) \approx A - B\tau. \quad (1)$$

The amount of power incident on the detector from a source with a fixed flux density is given by

$$P(\mathrm{W\,mJy^{-1}}) \propto 1 - \tau. \quad (2)$$

The calibration factor for converting the bolometer voltage to flux density on the sky is given by the product of these two factors:

$$C(\mathrm{V\,mJy^{-1}}) = (A - B\tau)(1 - \tau). \quad (3)$$

Because the resistance of the bolometer is also proportional to the optical depth, τ, we can use the bolometer output voltage level

to determine an empirical calibration scale that takes into account both intrinsic changes in the bolometer responsivity and changes in atmospheric transmission (see Laurent et al. 2005).

To measure the calibration curve for each bolometer, we make observations of sources of known flux density at different levels of sky loading and plot the DC level of each bolometer against a calibration factor calculated from the peak voltage in a map of the uncalibrated data. We fit a second-order polynomial to the measured calibration points. We expect the calibration to scale quadratically with the DC level of the bolometers when the optical depth is small (<0.2) because the calibration is a product of the linear change in responsivity with increased optical loading and the linear reduction in signal from the astronomical source due to increased atmospheric attenuation. We also measure the relative responsivities of the bolometers by comparing the response of the bolometers to the correlated variations in sky loading determined by averaging all of the bolometer time streams.

The calibration curves are not expected to change significantly over time for the same set of detectors, filters and optics. However, given that the previous set of data was taken in 2004 May, using a different scanning technique, we performed a full set of calibration observations roughly every 20 min during the science observations. These calibration sources were chosen to be close to the science observation target and included Mars, J0423−013, J0927+390, J1337−129 and 3C371.

The observations of the calibrators agree reasonably well with the 2004 May calibration curve which was based on observations of calibration sources with an estimated uncertainty of 10 per cent (Laurent et al. 2005). Because the optical depth during the 2006 observations was always below $\tau = 0.1$ we are not able to constrain the parameters for a second-order polynomial curve. Instead, we fit a relative amplitude of the jiggle-map calibration data to the polynomial curve determined from the 2004 May data of 1.0 ± 0.1 corresponding to a statistical rms variation of 10 per cent in the calibration scale factor. Given the variability of the sources in the 2006 calibration data, the deviations between the 2004 May calibration curve and the calibration sources measured with jiggle mapping were not considered to be great enough to warrant revising the calibration values and the May 2004 calibration parameters were used throughout. However, we include a systematic uncertainty of 12 per cent corresponding to the statistical error in the 2006 measurements combined with the estimated error (statistical and systematic) in the 2004 calibration.

3.4 Mapping

The result of the deconvolution and calibration procedure is a set of data vectors consisting of a measured flux density, f_i, an associated statistical error, σ_i, and sky coordinates, x_i and y_i, for all of the bolometers. The statistical error is computed from the rms variation of the bolometer signals both in phase and 90° out of phase with the chopper signal. Once maps had been made of the individual observations, they are co-added to produce a single image of Abell 1835 which is then convolved with a Gaussian point spread function with FWHM = 30.6 arcsec, corresponding to the best-fitting Gaussian to the Bolocam beam to identify sources in the map. The map in Fig. 3 clearly shows extended emission from the cluster as well as two point sources on either side. The point sources have been detected previously at 850 μm using the Submillimetre Common-User Bolometer Array (SCUBA) on the James Clerk Maxwell Telescope (Zemcov et al. 2007) as well as by Ivison et al. (2000). The characteristics of these point sources, as reported by Ivison et al. (2000), are given in Table 1.

Fig. 3 shows a map of the data calibrated in flux density. The map has been convolved with the Bolocam beam size to enhance the signal-to-noise ratio (S/N) for display purposes and therefore the effective beam size in the map is 42 arcsec. The peak flux density per beam in the map is approximately 14 mJy and the statistical error per beam in the centre of the map is approximately 2 mJy.

4 1.1-mm SKY MODEL FITTING

Analysis of the data from jiggle-map observations produces a map which consists of the astronomical emission filtered by a transfer function which is dominated by the effective chopped beam pattern (e.g. Fig. 2). This transfer function introduces negative lobes in the map for bright sources and reduces the apparent size and magnitude of emission from sources larger than the chop throw of 90 arcsec. Gaps in the maps of individual jiggle-map observations due to unresponsive bolometers in the array combined with sky rotation between different jiggle maps cause the transfer function to be non-uniform over the co-added map. In order to determine the most likely distribution of emission from known sources in the field, we produce a model for the astronomical emission including SZ from the cluster and dust emission from the point sources. We then put the model sky emission through the same scan strategy, pixel sampling and analysis pipeline as the real data in order to implement the same non-uniform transfer function on the model and the data. By comparing the processed model with the data, we determine parameters for the model that best fit the observed data.

4.1 Cluster profile and gas temperature

The SZ emission from the galaxy cluster was modelled assuming an isothermal beta radial profile:

$$\mathcal{F}(\theta_{\rm p}) = A\left(1 + \frac{\theta_{\rm p}}{\theta_{\rm c}}\right)^{\left(\frac{1}{2} - \frac{3\beta}{2}\right)}, \tag{4}$$

where $\mathcal{F}(\theta_{\rm p})$ is the flux density profile of the cluster as a function of projected angle $\theta_{\rm p}$, $\theta_{\rm c}$ and β are fitting parameters, A is a scaling parameter defined by

$$\mathrm{A} = \Delta\Omega I_0 y_0 g(x) \times 10^{26}\,\mathrm{Jy}. \tag{5}$$

Here, $\Delta\Omega$ is the solid angle of the pixels in the (model) map (the map was later convolved with the Bolocam beam such that the final flux density measurements were given in flux density beam^{-1}), $I_0 = \frac{2h}{c^2}(\frac{k_{\rm B}T_{\rm CMB}}{h})^3$ is the blackbody emission of the CMB at the redshift of the cluster, y_0 is the so-called 'Compton parameter' at the centre of the cluster (the Compton parameter in general, y, can be characterized as

$$y = \int n_{\rm e}\sigma_{\rm T}\frac{k_{\rm B}T_{\rm e}}{m_{\rm e}c^2}\mathrm{d}l, \tag{6}$$

where $n_{\rm e}$ and $T_{\rm e}$ are, respectively, the electron density and electron temperature along the line of sight), and $g(x)$ is a function that depends on the dimensionless frequency at which the observations are being made, $x = \frac{h\nu}{k_{\rm B}T_{\rm CMB}}$, as

$$g(x) = x^4\frac{e^x}{(e^x-1)^2}[x\coth(x/2) - 4]. \tag{7}$$

The temperature reported in the literature for Abell 1835 varies between approximately 6 and 12 keV (e.g. Allen & Fabian 1998; Peterson et al. 2001; Schmidt, Allen & Fabian 2001; Katayama

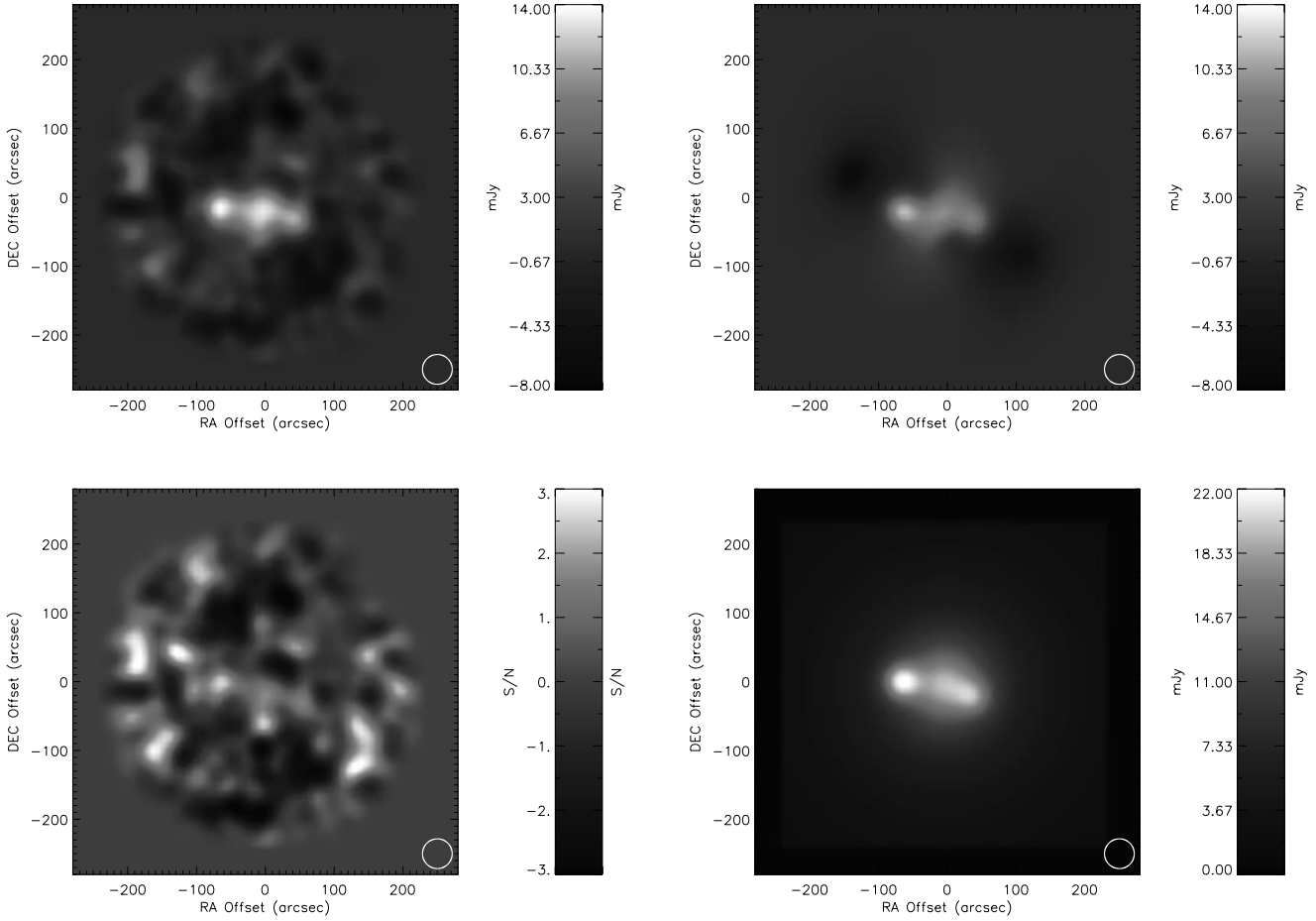

Figure 3. Top left: jiggle map of the raw Abell 1835 data convolved with the Bolocam beam so that the effective beam FWHM is 42 arcsec. Top right: simulated jiggle map of the best-fitting model consisting of the SZ emission ($\beta = 0.69$, $\theta_c = 33.6$ arcsec) and the two SCUBA point sources. The sky model has been convolved with the Bolocam beam once before performing the jiggle map and again afterwards so that the effective beam size is also 42 arcsec. The brightness scale of the signal and model are the same. Bottom left: S/N map of the residual map consisting of the raw data minus the best-fitting sky model map convolved with the Bolocam beam. The brightness scale has been magnified to cover the range $-3 < \sigma < +3$. Bottom right: map of the best-fitting three-parameter model before jiggle mapping. The model map has been convolved with the Bolocam beam twice so that the effective beam size is 42 arcsec. The brightness scale has been increased compared to the data and jiggle-map model by a factor of approximately 1.5.

Table 1. Point source positions and flux densities reproduced from Ivison et al. (2000).

Source id	RA (hh:mm:ss)	Dec. (dd:mm:ss)	850-μm flux density (mJy)	450-μm flux density (mJy)
SMM J14011+0252	14:01:04.7	+02:52:25	14.6 ± 1.8	41.9 ± 6.9
SMM J14009+0252	14:00:57.5	+02:52:49	15.6 ± 1.9	32.7 ± 8.9

& Hayashida 2004; LaRoque et al. 2006; Mantz et al. 2010). At these temperatures, relativistic corrections to the SZ can be on the order of 20 per cent and have to be taken into account during the analysis. For the results in this paper, we assume an isothermal gas with temperature $T_e = 9$ keV and apply the formula for relativistic corrections to the expected SZ thermal signal from Itoh, Kohyama & Nozawa (1998), up to fifth order in θ, where

$$\theta = \frac{k_B T_e}{m_e c^2}. \quad (8)$$

4.2 Sky model parameters

The free parameters of the model were the cluster geometry (θ_c and β), the Comptonization (y_0) and the flux densities of the two point sources $\mathcal{F}_1$ and $\mathcal{F}_2$ (corresponding to SMM J014011+0252 and SMM J14009+0252, respectively). We also allowed the centre of the SZ emission from the cluster to be offset from the X-ray centre in RA (RA offset) and Dec. (Dec. offset). Finally, for some models, we included emission from a point source located at the position of the brightest cluster galaxy (BCG) at the centre of the cluster ($\mathcal{F}_2$). For each set of parameters, we produced a high-resolution map with pixel size of 1 arcsec. This map was then convolved with the Bolocam beam to produce a simulated map of the cluster at the resolution of the telescope. This in turn was then observed by using the RA and Dec. values from the data stream along with the chopping and nodding pattern to produce a simulation of what we expect to observe in the data map given the assumed values of flux density (for the point sources) and y_0. Finally, the chopped map was rebinned to the same pixel size as the raw data maps. By comparing

the model maps corresponding to different values of the parameters with the data, we constructed a multiparameter likelihood space, which we then searched to extract the best-fitting models and corresponding parameter set which minimized the χ^2 difference between the model map and the data map. All of the comparisons between the models and the data were done without reconvolving the maps with the Bolocam beam. Fig. 3 shows maps of the best-fitting model before and after being put through the observation and analysis pipeline which simulates the transfer function present in the data map. The effect of the jiggle-map observations and data processing (i) reduces the observed flux from all of the sources, (ii) reduces the observed extent of the cluster, particularly along the chop direction and (iii) creates negative lobes on either side of the sources.

Generally, SZ experiments are not able to constrain the parameters θ_c and β, since the resolution of most SZ experiments is comparable to the size of the cluster extended emission and X-ray observations are commonly used to derive cluster shape parameters. However, Hallman et al. (2007) have suggested that using X-ray derived profiles for fitting SZ observations can lead to bias in the derived values of y. In addition, Abell 1835 has a central cooling flow which leads to a sharp peak in the X-ray emission at the centre and for this reason a single isothermal beta model fit to all the X-ray data in a set of observations is not suitable. Because of this, the values of the profile parameters for Abell 1835 found in the literature can vary considerably (see e.g. values reported in Peterson et al. 2001; Schmidt et al. 2001; Jia et al. 2004; Zemcov et al. 2007).

We adopt values for θ_c and β obtained using *Chandra* X-ray data and interferometric SZ data from the Owens Valley Radio Observatory (OVRO) and the Berkeley Illinois Maryland Association (BIMA) from LaRoque et al. (2006). One set of cluster profile parameters is derived from a joint fit to the X-ray data excluding the region within 100 kpc of the X-ray centre and the SZ data (hereafter LaRoque X-ray+SZ). The second set of cluster profile parameters is derived from the SZ data alone (hereafter LaRoque SZ only). It is possible to use the entire SZ data set to fit the cluster profile since SZ emission has a weaker dependence upon electron density than X-ray observations, and the SZ profile is not expected to be significantly affected by the presence of cooling flows (Motl et al. 2005). The values of θ and β for the LaRoque X-ray+SZ data are $\beta = 0.69$, $\theta_c = 33.6$ arcsec, and for the LaRoque SZ-only data: $\beta = 0.70$, $\theta_c = 50.1$ arcsec.

4.3 Dust emission from brightest cluster galaxy

At mm and submm wavelengths, the contribution from dust emission from cluster galaxies and background galaxies is a source of confusion. In addition to the bright lensed galaxies on either side of the cluster centre, the cluster's BCG exhibits significant CO emission which is a standard tracer of dust. Edge et al. (1999) reports a flux density of 20 ± 5 mJy for continuum emission at $\lambda = 450\,\mu$m from the central cluster galaxy, while Zemcov et al. (2007) reports a 450-μm flux density of -2 ± 13 mJy.

Assuming that all of the emission reported by Edge et al. (1999) at 450 and 850 μm is attributed to dust in the BCG, we can fit a greybody spectrum to the submm data, assuming a dust temperature $\sim$30 K and an emissivity which varies as $\nu^{1.5}$. The flux density of the cD galaxy at 1.1 mm using this model is expected to be $\sim 1.8 \pm 0.5$ mJy. This value is consistent with the spectral energy distribution (SED) produced for Abell 1835's BCG reported by Egami et al. (2006) and is used in combination with the LaRoque cluster profile for one of the models.

4.4 Model fitting procedure

We computed the χ^2 for a set of models in a multiparameter space either fixing the values of both β and θ_c or allowing one of the parameters to vary. Specifically, we used the following combinations of fixed profile parameters: ($\beta = 0.69$, $\theta_c = 33.6$ arcsec); ($\beta = 0.69$, $\theta_c = 50.1$ arcsec); $\beta = 0.69$; $\theta = 33.6$ and 50.1 arcsec.

The χ^2 for a given model was defined as

$$\chi^2 = \sum_i \frac{(d_i - m_i)^2}{\sigma_i^2}, \tag{9}$$

where d_i denotes the signal in pixel i of the data map, m_i represents the signal in pixel i of the model map, and σ_i is the noise in pixel i of the noise map. The best-fitting parameters for a given analysis run were those that minimized this value of χ^2.

4.5 Results and statistical uncertainty of model parameters

The results from the comparison of the 1.1-mm data to the sky models are given in Table 2. Errors on the values of the fit parameters were found by computing the inverse of the Fisher matrix of the χ^2 values of the data compared to models with different parameter values and evaluating its diagonal elements. For parameters with a Gaussian distribution, the Fisher matrix F_{ij} is given by

$$F_{ij} = \frac{1}{2}\left(\frac{\partial^2 \chi^2}{\partial p_i \partial p_j}\right), \tag{10}$$

where p_i represents the vector of parameters being fitted, and the second-order differential is evaluated at the value of p at which the χ^2 value is minimized.

Table 2. Parameter estimates (1.1-mm Bolocam observations) and χ^2 values; number of degrees of freedom = 3013. (f) denotes the cluster profile parameters which were fixed for the model. $\mathcal{F}_0$ is the flux density in mJy for a point source at the position of the BCG. The y_0 values assume an isothermal cluster gas with temperature, $T_e = 9$ keV.

Model parameters						
β	0.69 (f)	0.69 (f)	0.69 (f)	1.20 ± 0.2	1.60 ± 0.2	0.69 (f)
θ_c (arcsec)	33.6 (f)	50.1 (f)	$14.7^{+2.4}_{-2.2}$	33.6 (f)	50.1 (f)	33.6 (f)
$\mathcal{F}_0$	0.0	0.0	0.0	0.0	0.0	1.8
$\mathcal{F}_1$ (mJy)	6.48 ± 2.00	6.22 ± 2.08	7.16 ± 1.88	7.09 ± 1.89	7.17 ± 1.84	6.48 ± 2.00
$\mathcal{F}_2$ (mJy)	11.32 ± 1.92	10.90 ± 1.98	11.98 ± 1.79	12.38 ± 1.82	12.18 ± 1.77	11.32 ± 1.92
y_0 ($\times 10^{-4}$)	(4.76 ± 0.49)	(4.50 ± 0.49)	(6.63 ± 0.64)	(4.93 ± 0.47)	(4.26 ± 0.40)	(4.41 ± 0.52)
RA offset (arcsec)	1.8	1.9	2.1	2.1	2.0	2.0
Dec. offset (arcsec)	3.6	3.9	2.6	2.8	2.5	3.4
χ^2	3066	3079	3058	3056	3054	3062

The components of F_{ij} were evaluated from an array of χ^2 values for model parameters around the minimum values. The results of this analysis are shown in Table 2. The accuracy of the estimate of the χ^2 for a given model relies on an accurate noise model for the data. The noise was calculated from the rms variation in the raw data which contributed to the final signal in each pixel assuming no covariance between pixels. The level of covariance is expected to be low due to the chopping, and because the only cleaning of the data involves an average subtraction. Jackknife maps were also made to check these assumptions by multiplying the individual raw data points by ± 1 randomly before co-adding. The resulting noise maps agreed with the noise estimates made from the signal maps.

Overall, the 1.1-mm data is well fitted by the models described in Table 2. The models where one of the cluster profile parameters (either θ_c or β) is allowed to vary have the lowest χ^2 values. The best-fitting parameters for these models correspond to a steeper cluster profile than the profiles found by LaRoque et al. (2006). This could be due to confusion from dust emission from the central galaxy in the cluster, as the model which includes a fixed point source has a lower χ^2 than the models with fixed θ_c and β and no point source. For models with fixed cluster profiles, the measured values of the central Comptonization vary from $y_0 = 4.41 \times 10^{-4}$ to 4.76×10^{-4} which is within the 1σ statistical errors. For all models, the best-fitting values for the point source flux densities vary by less than the 1σ statistical errors. The errors on the values of parameters in Table 2 include statistical errors as well as errors due to pointing and uncertainty in the model parameters. They do not include systematic errors which are discussed below.

4.6 Validity of sky model and noise properties of the map

In order to reliably simulate the chopped observations, all sources in the field need to be included in the sky model. The map of the $\beta = 0.69, \theta_c = 33.6$ arcsec model is also shown in Fig. 3, convolved with the Bolocam beam. The final map in Fig. 3 displays the difference between the model map and the raw data, convolved with the Bolocam beam to emphasize any differences between them. The difference map shows upon inspection that the cluster signal and the point sources have been removed effectively and that, therefore, the model is a reasonable simulation of the data.

Fig. 4 shows a histogram of the difference between the S/N data map and the simulated map. The Gaussian form of the histogram is consistent with the residual signal being dominated by noise rather than other point sources. The histogram has a standard deviation of 1.01, indicating that the noise has been correctly estimated. There may be some suggestion of deviation in the high S/N region between the histogram and the fit, but this can be attributed to regions of lower coverage in the outer sections of the map.

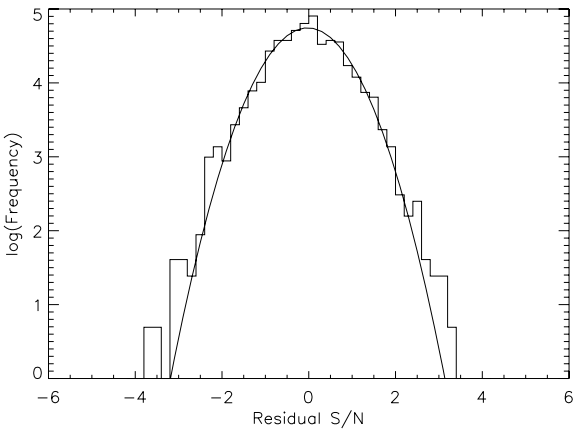

Figure 4. S/N histogram of the residual map obtained by subtracting the best-fitting model with fixed $\beta = 0.69$ and $\theta_c = 33.6$ arcsec from the data, plotted on a logarithmic scale. The Gaussian best fit to the histogram (the solid line in the log plot) has $\sigma = 1.01$.

We also test for the presence of spatially correlated noise in the maps by computing the two-point correlation function of the S/N maps of the jackknife data and of the data minus the best-fitting model. The two-point correlation function ω_{ij} is given by

$$\omega_{ij} = \sum_{i',j'} \frac{(d_{i'j'} \times d_{i'-i,j'-j})}{\sigma_{i'j'}\sigma_{i'-i,j'-j}}, \tag{11}$$

where d_{ij} and σ_{ij} are the data and noise from the map in the pixel with separation in RA denoted by the index i and separation in Dec. denoted by the index, j. For comparison, we also generate a map with white noise Gaussian distributed around zero mean with an rms of 1 and apply the coverage mask to this data and compute the two-point correlation function as above. Fig. 5 (top) shows maps of the raw S/N for (i) white noise, (ii) the residual map consisting of the data minus the best-fitting sky model and (iii) the jackknife map. For each set of data, the peak value at the centre pixel of the autocorrelation map is approximately equal to $\omega_{00} = N$, where N is the number of good pixels in the coverage mask. If there is no correlated noise present, then the average value of all of the other pixels in the autocorrelation map should be equal to zero with an rms variation of $\sigma_{ij} = \sqrt{N_{ij}}$, where N_{ij} is the number of pixels used to compute each value of ω_{ij}. Because of the limited coverage, the value of N_{ij} decreases as the separation between pixels in the computation of ω_{ij} increases. In order to best identify sky correlations, we normalize the autocorrelation function by $\sqrt{N_{ij}}$. This gives maps which should still have an average value of zero with an rms value of 1 for each pixel element other than the central pixel. Fig. 5 (bottom) shows maps of the two-point correlation functions for each of the noise maps. The peak value at the centre of each map is $\omega_{00} \approx \sqrt{N_0 0} = \sqrt{1729} = 41.5$, but we have limited the scale to a maximum of nine in order to be able to see the residual fluctuations outside of the central pixel. Finally, we exclude the central pixel and smooth the autocorrelation maps to the Bolocam beam size of 30.6 arcsec. If correlated noise is present at angular scales larger than the Bolocam beam, we should see an increase in the rms of smoothed maps of the two-point correlation functions compared to the rms of the unsmoothed maps.

In the reference white noise map, we find a residual rms of $\sigma = 0.86$ for the smoothed two-point correlation function map compared to an rms of $\sigma = 1.03$ for the unsmoothed map excluding the central pixel. In the map of the two-point correlation function for the jackknife data, we find an rms value of $\sigma = 0.82$ for the smoothed two-point correlation function map compared to an rms of $\sigma = 1.15$ for the unsmoothed map excluding the central pixel. Finally, for the residual S/N map corresponding to the difference between the raw data and the best-fitting model, we find a residual rms of $\sigma = 1.155$ for the smoothed two-point correlation function map compared to an rms of $\sigma = 0.94$ for the unsmoothed map excluding the central pixel. The number of independent beams in the smoothed maps is approximately 60, so the expected variation in the rms values is approximately 12 per cent. We therefore place an upper limit on the level of correlated noise in the map at approximately 15 per cent of the white noise level.

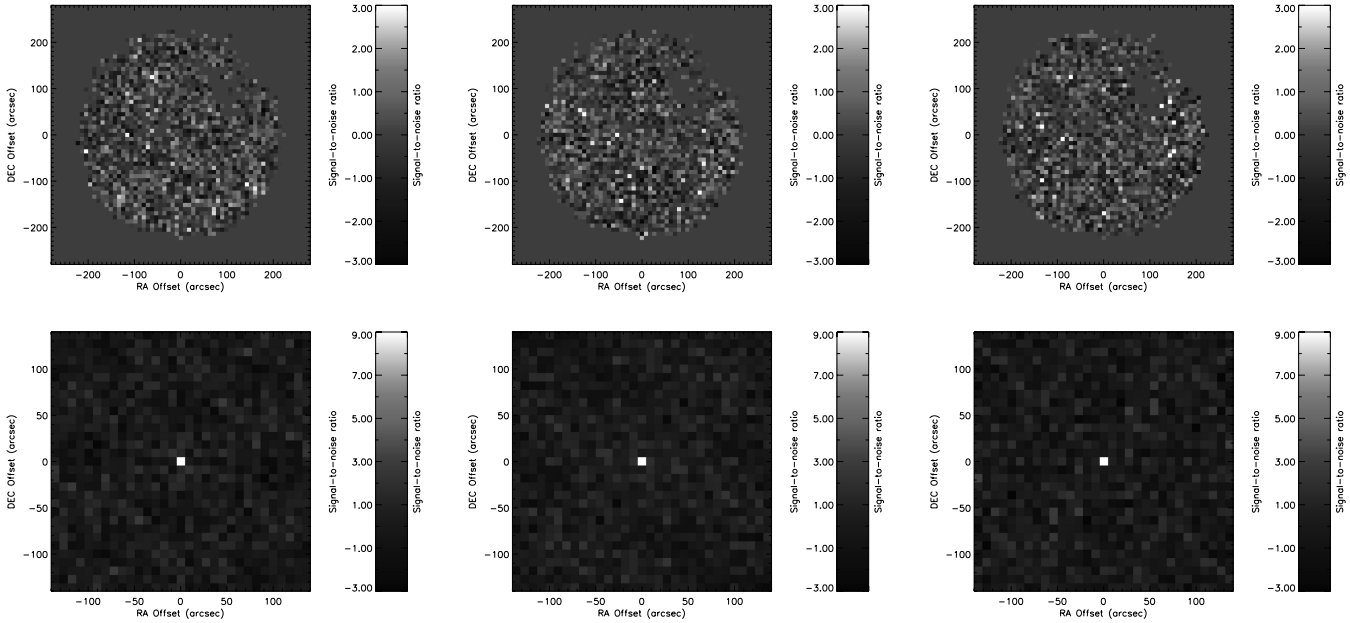

Figure 5. Top left: map of simulated Gaussian distributed white noise with zero mean and an rms of 1. The noise has been multiplied by the coverage mask used in the A1835 observations. Top middle: S/N map of residual noise from the A1835 raw data map minus the best-fitting sky model. The residual signal has been divided by the error in each pixel. Top right: S/N map of the jackknife data. Bottom left: map of the autocorrelation function for the simulated white-noise map shown above. The peak signal in the centre is 41.5 corresponding to the square root of the number of good pixels identified in the coverage mask. The scale has been limited to a maximum of nine in order to show the variations of the off-centre pixels. In the presence of correlated noise, we would expect to see significant signals away from the centre pixel. Bottom middle: map of the autocorrelation function for the residual S/N map. There is no obvious evidence for the presence of correlated noise or residual signal at the level of the white noise in the map. Bottom right: map of the autocorrelation function for the jackknife map. There is no evidence for the presence of correlated noise. All maps are made with pixel sizes of 9 arcsec and have not been convolved with the Bolocam beam.

5 SZ SIGNAL AND SPECTRUM

5.1 Results from 1.1-mm data

Assuming that all of the flux density measured at 1.1 mm from the cluster is from the SZ thermal effect, we estimate values of y_0 ranging from 4.19×10^{-4} to 6.52×10^{-4} for the different cluster models. Variations in y_0 are strongly linked to variations in the cluster profile parameters as the observed flux density from the cluster centre is an integral of the cluster emission profile over the beam solid angle. It is therefore appropriate to consider errors in y_0 associated with particular values of θ_c and β. The significance of the measured value of y_0 for any of the models used for fitting parameters corresponds to a detection the SZ increment in Abell 1835 with a significance of $\sim 10\sigma$. This is one of the highest significance detections of a cluster in the positive region of the SZ spectrum to date.

5.2 y_0 and v_z estimates from multifrequency data

A plot of the SZ spectrum of Abell 1835 from this measurement and other SZ measurements in the literature (Mauskopf et al. 2000; LaRoque et al. 2006; Sayers et al. 2011) is given in Fig. 6. All of the measurement values have been converted to values for the central intensity, $I_{\rm central}$, for a cluster with the same emission profile. This has been done by computing the central flux density per beam from each instrument given quoted values of y_0, v_z and the associated cluster model parameters, and then computing the equivalent value

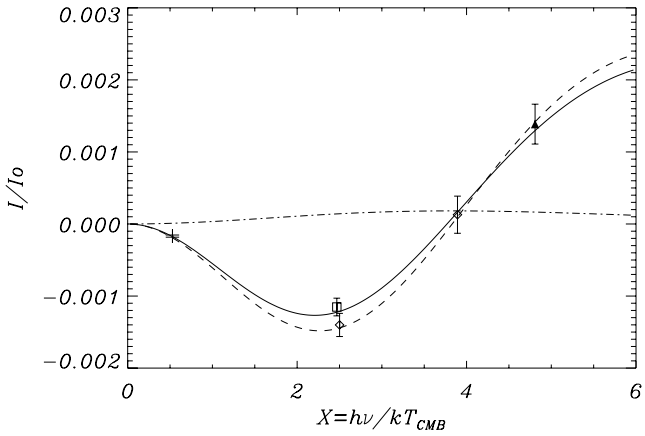

Figure 6. The SZ spectrum of Abell 1835. The 30-GHz results (no symbol, $x \sim 0.5$) are taken from LaRoque et al. (2006). The point at 140 GHz (open square, $x \sim 2.5$) is from Sayers et al. (2011). The points at 142 and 221 GHz (open diamonds) are from Mauskopf et al. (2000), while the filled triangle ($x \sim 4.8$) represents the results reported here. All points have been renormalized to the central intensity of a source with emission profile corresponding to the parameters $\theta_c = 33.6$ arcsec and $\beta = 0.69$. The solid curve is the best-fitting SZ spectrum with $y_0 = 3.58 \times 10^{-4}$ and $v_z = -537\,{\rm km\,s^{-1}}$. The dashed curve shows the central intensity for a non-relativistic SZ thermal spectrum with $y_0 = 3.58 \times 10^{-4}$ and zero peculiar velocity while the dot–dashed curve shows the central intensity of the peculiar velocity distortion alone with $v_z = -537\,{\rm km\,s^{-1}}$.

of $I_{\rm central}$ required to give the same flux density for a cluster with profile corresponding to $\theta_{\rm c} = 33.6$ arcsec and $\beta = 0.69$.

For the 1.1-mm data, we use the central intensity from the SZ model which includes a point source at the position of the central galaxy with a best-fitting value for y_0 of $(4.41 \pm 0.53) \times 10^{-4}$, with a $\chi^2 = 3062$. This corresponds to a central intensity for the cluster emission of $I_{\rm c} = 3.73 \times 10^{-21}\,{\rm W\,m^{-2}sr^{-1}\,Hz^{-1}}$.

For the 2.1-mm data from Sayers et al. (2011), we performed a simultaneous fit for the cluster profile and the two point sources similar to the analysis performed on the 1.1-mm data. Assuming zero peculiar velocity and an electron temperature of $T_{\rm e} = 9$ keV, we find best-fitting values from the 2.1-mm data alone of $y_0 = 3.04 \pm 0.28 \pm 0.15 \times 10^{-4}$, where the first error is the statistical error and the second error is due to uncertainty in the flux calibration. The best-fitting flux values for the point sources at 2.1 mm are 0 ± 1.4 mJy for SMJ14011+0252 and 5 ± 1.4 mJy for SMJ14009+0252. In addition to the inclusion of the point sources in the sky model, there were other minor changes in the calibration of the 2.1-mm data compared to the results presented in Sayers et al. (2011) which slightly reduced the calibration uncertainty.

We then fit the values for the central intensity of the emission with the form of the cluster profile at different wavelengths to a spectrum that includes contributions from the non-relativistic kinematic effect and the relativistic thermal effect. The kinematic effect has the form:

$$I_{\rm kinetic} = -\tau_{\rm e}\frac{v_z}{c}h(x), \tag{12}$$

where $\tau_{\rm e}$ is the optical depth of the cluster gas, given by $y_0(\frac{mc^2}{k_{\rm B}T_{\rm e}})$, v_z is the peculiar velocity of the galaxy cluster and $h(x) = x^4\frac{e^x}{(e^x-1)^2}$.

The best-fitting values for y_0 and v_z to the SZ spectrum were found to be $y_0 = (3.58 \pm 0.28) \times 10^{-4}$, and $v_z = -537 \pm 414\,{\rm km\,s^{-1}}$ assuming an isothermal gas with temperature $T_{\rm e} = 9$ keV. This is consistent with previous measurements of v_z for Abell 1835 (Mauskopf et al. 2000; Benson et al. 2003) and represents the most sensitive test for peculiar velocity in an individual galaxy cluster using the SZ effect to date.

5.3 Sources of systematic error

5.3.1 Calibration

We estimated the calibration error from the noise-weighted dispersion of the measured point flux densities relative to the 2004 May model. This gives a calibration error of 10 per cent, which combined with the uncertainty in the 2004 May model (Laurent et al. 2005) gives an overall calibration error of 12 per cent.

5.3.2 Kinematic effect

The kinematic SZ effect introduces a correction to the measurement of the central Comptonization that depends on the cluster peculiar velocity. Concordance cosmology predicts an rms peculiar velocity of around $300\,{\rm km\,s^{-1}}$ (Bhattacharya & Kosowsky 2007). A velocity this high at 275 GHz produces a kinematic effect that is approximately 9 per cent of the thermal effect. We include this as a source of systematic error in the measurement of y_0 from the 1.1-mm data alone but not in the measurement of the 1.1-mm central surface brightness. This can be constrained by combining data from SZ measurements at different wavelengths.

5.3.3 Astrophysical confusion

The most significant sources of confusion in observations of the SZ effect are the CMB and dusty galaxies. Typical CMB temperature anisotropy signals based on the current concordance model spectrum were simulated and observed using the same scan strategy as for the Abell 1835 observations. These produced an rms amplitude for the cluster models used in the SZ analysis equivalent to a 1.5 per cent error in the measured central surface brightness. Dusty galaxies at 1.1 mm contribute an rms signal of approximately 0.5 mJy (e.g. Blain 1998), which corresponds to a 5.4 per cent error in the measured cluster amplitude at 1.1 mm.

We find that the flux density of SMM J14011+252 scales according to a power law between 850 μm and 1.1 mm as approximately ν^3 while SMM J14009+0252 scales as approximately ν^2. If we scale with these indices from the 1.1-mm flux density to the lower frequencies, we find flux density values of 3 and 7 mJy at 1.4 mm and 1 mJy and 3 mJy at 2.1 mm. These flux densities are consistent with the values derived from the Bolocam 2.1-mm data. The measured flux density from the Abell 1835 observations with the Sunyaev–Zel'dovich Infrared Experiment (SuZIE) in the central 1.7-arcmin beam was 9 mJy at 221 GHz and −42 mJy at 145 GHz. The two point sources are separated by approximately 2 arcmin in RA so the effect on scans with a 1.7-arcmin FHWM beam across the cluster in Dec. would be to increase the central flux density by approximately 40 per cent of the total point source flux density, whilst scans across the cluster in RA would also increase the observed core radius of the cluster. If we assume that the model fits are dominated by the central pixel and that the SuZIE scans were primarily not aligned in RA, then we find a maximum correction to the measured flux density of 4 mJy or 45 per cent of the central intensity at 221 GHz and 2 mJy or 2.5 per cent of the central intensity at 2.1 mm. We include these errors in the data points from SuZIE.

5.3.4 Physical model uncertainties

For the calculation of the Comptonization and peculiar velocity, we assume that the cluster gas is isothermal with a temperature of 9 ± 3 keV which broadly agrees with deprojections of X-ray measurements from *Chandra* and *XMM* (Schmidt et al. 2001; Sanders et al. 2010). Uncertainties in the electron gas temperature of 30 per cent contribute a 10 per cent error in the amplitude of the peculiar velocity signal (but not in the S/N of a peculiar velocity measurement) and also contribute to an error in the estimate of y_0 of up to ∼3 per cent due to relativistic corrections to the SZ thermal spectrum and intensity. As we have seen in the model fitting, variations in derived values of y_0 are strongly linked to the cluster profile parameters, therefore we consider errors in y_0 associated with particular values of $\theta_{\rm c}$ and β, and do not include these as sources of error in the measured flux density.

A breakdown of the error budget for the observations presented here is given in Table 3.

6 CONCLUSIONS

The observation and analysis of 1.1-mm Bolocam jiggle-map data of Abell 1835, including details of the process of converting the raw data to maps of the cluster, have been discussed. A parameter search has been used to determine the best-fitting values of the central surface brightness of the cluster emission and the flux densities of the point sources SMM J14011+0252 and SMM J14009+0252. These values are found to be $I_{\rm c} = 3.73 \pm 0.45 \pm 0.60 \times 10^{-21}\,{\rm W\,m^{-2}sr^{-1}\,Hz^{-1}}$, $6.5 \pm 2.0 \pm 0.8$ mJy and $11.3 \pm 1.9 \pm 1.3$ mJy, respectively, with a statistical S/N of 8.3, 3.3 and 6.0, respectively. Assuming an isothermal cluster gas with $T_{\rm e} =$

Table 3. Top: uncertainty in central surface brightness for the cluster emission model in Table 2 with $\theta_c = 33.6$ arcsec and $\beta = 0.69$ from 1.1-mm observations of Abell 1835. The best-fitting central surface brightness value for this model given the data is $I_c = 3.73 \times 10^{-21}$ W m^{-2}sr^{-1} Hz^{-1} assuming a flux density for the central galaxy of 1.8 mJy. Middle: uncertainty in the determination of the central Comptonization, y_0, for Abell 1835 from the two-parameter fit to the multifrequency data. The cluster gas temperature uncertainty assumes a conservative estimate of $T_e = 9 \pm 3$ keV. The best-fitting value for the central Comptonization for $T_e = 9$ keV is $y_0 = 3.58 \times 10^{-4}$. Bottom: uncertainty in the determination of the cluster peculiar velocity, v_z, scaled by the cluster optical depth, $\tau_e = y_0(m_e c^2/kT_e)$. The best-fitting value for the peculiar velocity for $T_e = 9$ keV is $\tau_e(v_z/c) = 10.9$ which corresponds to $v_z = -537$ km s^{-1}. The statistical uncertainty in the fit for both y_0 and v_z includes the statistical and calibration uncertainty for each measurement.

Source of uncertainty	Central surface brightness (10^{-21} W m^{-2}sr^{-1} Hz^{-1})
Statistical uncertainty	0.45
Calibration	0.45
CMB confusion	0.03
Dusty lensed galaxies	0.2
BCG dust emission	0.27
Uncertainty in y_0 from spectral fit	Δy_0 ($\times 10^{-4}$)
Statistical uncertainty	0.28
Cluster gas temperature	0.11
Error in v_z from spectral fit	$\Delta(\tau_e \frac{v_z}{c})$
Statistical uncertainty	8.4
Cluster gas temperature	1.9

9 keV and zero peculiar velocity, this emission corresponds to an SZ increment with a Compton parameter for the cluster of $y_0 = (4.41 \pm 0.53 \pm 0.70) \times 10^{-4}$. We fit a SED to the measured central surface brightness values for Abell 1835 using a fiducial cluster gas distribution model over a frequency range from 30 to 275 GHz, including both thermal and kinetic SZ effects and relativistic corrections to the SZ effect up to fifth order. The best-fitting values of y_0 and v_z were found to be $(3.58 \pm 0.28 \pm 0.11) \times 10^{-4}$ and $-537 \pm 414 \pm 93$ km s^{-1}, where the first error term is the uncertainty in the fit and the second error term corresponds to uncertainty in the intracluster gas temperature. In order to better separate the effects of relativistic cluster gas and peculiar velocity as well as evaluate the contamination from point sources in the same field as the cluster, more data need to be obtained at shorter wavelengths.

ACKNOWLEDGMENTS

This work was supported by NSF grants AST-9980846 and AST-0206158 and by STFC grants XXX. We wish to acknowledge M. Zemcov for providing access to SCUBA archive data and for useful discussion, which improved the content of this paper significantly. We would also like to recognize and acknowledge the cultural role and reverence that the summit of Mauna Kea has within the Hawaiian community. We are fortunate and privileged to be able to conduct observations from this mountain.

REFERENCES

Albrecht A., Bernstein G., 2007, Phys. Rev. D, 75, 103003
Allen S. W., Fabian A. C., 1998, MNRAS, 297, L57
Battistelli E. S. et al., 2006, ApJ, 645, 826
Benson B. A. et al., 2003, ApJ, 592, 674
Benson B. A., Church S. E., Ade P. A. R., Bock J. J., Ganga K. M., Henson C. N., Thompson K. L., 2004, ApJ, 617, 829
Bhattacharya S., Kosowsky A., 2008, Phys. Rev. D, 77, 300
Birkinshaw M., 1999, Phys. Rep., 310, 97
Birkinshaw M., Hughes J. P., Arnaud K. A., 1991, ApJ, 376, 466
Blain A. W., 1998, MNRAS, 297, 502
Bonamente M., Joy M. K., LaRoque S. J., Carlstrom J. E., Reese E. D., Dawson K. S., 2006, ApJ, 647, 27
Carlstrom J. E., Holder G. P., Reese E. D., 2002, ARA&A, 40, 643
DeDeo S., Spergel D. N., Trac H., 2005, preprint (arXiv:astro-ph/0511060)
Diego J. M., Martinez-Gonzalez E., Sanz J. L., Benitez N., Silk J., 2002, MNRAS, 331, 556
Edge A. C., Ivison R. J., Smail I., Blain A. W., Kneib J.-P., 1999, MNRAS, 306, 599
Egami E. et al., 2006, ApJ, 647, 922
Enoch M. L. et al., 2006, ApJ, 638, 293
Glenn J. et al., 1998, Proc. SPIE, 3357, 326
Grainge K., 1996, PhD thesis, Cambridge University
Grego L., Carlstrom J. E., Reese E. D., Holder G. P., Holzapfel W. L., Joy M. K., Mohr J., Patel S., 2001, ApJ, 552, 2
Haig D. J. et al., 2004, Proc. SPIE, 5498, 78
Hallman E. J., Burns J. O., Motl P. M., Norman M. L., 2007, ApJ, 665, 911
High F. W. et al., 2010, ApJ, 723, 1736
Hincks A. D. et al., 2010, ApJS, 191, 423
Holzapfel W. L. et al., 1997, ApJ, 480, 449
Itoh N., Kohyama Y., Nozawa S., 1998, ApJ, 502, 7
Ivison R. J., Smail I., Barger A. J., Kneib J.-P., Blain A. W., Owen F. N., Kerr T. H., Cowie L. L., 2000, MNRAS, 315, 209
Jia S. M., Chen Y., Lu F. J., Chen L., Xiang F., 2004, A&A, 423, 65
Jones M., 1995, Astrophys. Lett. Commun., 32, 347
Katayama H., Hayashida K., 2004, Advances Space Res., 34, 2519
LaRoque S. J., Bonamente M., Carlstrom J. E., Joy M. K., Nagai D., Reese E. D., Dawson K. S., 2006, ApJ, 652, 917
Laurent G. T. et al., 2005, ApJ, 623, 742
Mantz A., Allen S. W., Ebeling H., Rapetti D., Drlica-Wagner A., 2010, MNRAS, 406, 1773
Marriage T. et al., 2011, ApJ, 737, 61
Mauskopf P. D. et al., 2000, ApJ, 538, 505
Motl P. M., Hallman E. J., Burns J. O., Norman M. L., 2005, ApJ, 623, L63
Peterson J. R. et al., 2001, A&A, 365, L104
Plagge T., Benson B. A., Ade P. A. R., Aird K. A., Bleem L. E., 2010, ApJ, 716, 1118
Reese E. D., 2003, in Freedman W. L., ed., Carnegie Obser. Astrophys. Ser. Vol. 2, Measuring and Modeling the Universe. Cambridge Univ. Press, Cambridge, p. 138
Rephaeli Y., Sadeh S., Shimon M., 2005, in Melchiorri F., Rephaeli Y., eds, Background Microwave Radiation and Intracluster Cosmology: The Sunyaev–Zeldovich Effect. IOS Press, the Netherlands; Società Italiana di Fisica, Bologna, Italy, p. 57
Sanders J. S., Fabian A. C, Smith R. K., Peterson J. R., 2010, MNRAS, 402, 11
Sayers J. et al., 2010, ApJ, 708, 1674
Sayers J., Golwala S. R., Ameglio S., Pierpaoli E., 2011, ApJ, 728, 39
Schmidt R. W., Allen S. W., Fabian A. C., 2001, MNRAS, 327, 1057
Sunyaev R. A., Zel'dovich Ya. B., 1970, Ap&SS, 7, 3
Tsuboi M., Miyazaki A., Kasuga T., Matsuo H., Kuno N., 1998, PASJ, 50, 169
Udomprasert P. S., Mason B. S., Readhead A. C. S., Pearson T. J., 2004, ApJ, 615, 63
Vanderlinde K. et al., 2010, ApJ, 722, 1180
Weller J., Battye R. A., Kneissl R., 2002, Phys. Rev. Lett., 88, 231301
Williamson R. et al., 2011, ApJ, 738, 139
Zemcov M., Borys C., Halpern M., Mauskopf P. D., Scott D., 2007, MNRAS, 376, 1073

This paper has been typeset from a TEX/LATEX file prepared by the author.